

Corrugated aluminum nitride energy harvesters for high energy conversion effectiveness

This article has been downloaded from IOPscience. Please scroll down to see the full text article.

2011 J. Micromech. Microeng. 21 085037

(<http://iopscience.iop.org/0960-1317/21/8/085037>)

View [the table of contents for this issue](#), or go to the [journal homepage](#) for more

Download details:

IP Address: 169.229.32.136

The article was downloaded on 17/08/2011 at 21:02

Please note that [terms and conditions apply](#).

Corrugated aluminum nitride energy harvesters for high energy conversion effectiveness

Ting-Ta Yen¹, Taku Hirasawa, Paul K Wright, Albert P Pisano and Liwei Lin

Berkeley Sensor and Actuator Center, University of California at Berkeley, CA, USA

E-mail: tyen@eecs.berkeley.edu

Received 12 April 2011, in final form 14 June 2011

Published 26 July 2011

Online at stacks.iop.org/JMM/21/085037

Abstract

Aluminum nitride energy harvesters based on corrugated cantilever structures have been proposed, designed and demonstrated by means of micromachining processes with high energy conversion effectiveness. Corrugated cantilever design with a single piezoelectric layer prevents the common problem of an energy cancellation issue in a piezoelectric cantilever, by using a simple fabrication process similar to those in making the unimorph energy harvesters. Furthermore, corrugated structure can have an energy conversion effectiveness comparable to a conventional bimorph design. Experimentally, a prototype energy harvester with measured resonance frequency of 2.56 kHz has been fabricated. Under an input acceleration of 0.25 G, the amplitude of output voltage from the energy harvester has been recorded as 92 mV at a load resistance of 0.86 M Ω and the calculated output power is 4.9 nW. Furthermore, a multifold device resonating at 853 Hz with output power of 0.17 μ W under acceleration of 1 G has been recorded.

(Some figures in this article are in colour only in the electronic version)

1. Introduction

Alternative energy solutions to replace batteries from sustainable power resources have attracted great interests in recent years since the application of energy harvesters in a variety of devices could provide long-term sustainability [1]. In particular, micro- and nano-scale sensors typically require low power to operate, and small-size energy harvesters could be suitable power sources. For example, piezoelectric energy harvesters have been proposed in remote sensing systems by scavenging vibration energy from the surrounding environments [2]. The piezoelectric effect has been selected over other means of energy conversion such as electrostatic or electromagnetic mechanisms because higher energy conversion effectiveness can be achieved [3]. Schematically, piezoelectric energy harvesters have the common design of a cantilever beam structure with a proof mass driven by different piezoelectric structural designs such as unimorph or bimorph

configurations [4–6]. In the unimorph design, the strain energy in the bottom base layer could not be easily converted into electrical energy, since it could cancel out the energy generated from the top piezoelectric layer. Possible energy generation from the base layer is either left uncollected in the unimorph design or collected by using the bimorph design. Therefore, the energy harvesters based on the unimorph designs typically have lower energy conversion effectiveness as compared with those based on the bimorph designs. However, it is noted that most micro energy harvesters fabricated by micromachining technologies [7] have used the unimorph designs. The reason is to avoid complicated manufacturing processes required for bimorph designs. Clearly, it would be desirable to have micro energy harvesters based on a simple micromachining process with good energy conversion effectiveness.

Material properties also play an important role in energy harvesters, since piezoelectric properties directly affect the energy conversion effectiveness. Different piezoelectric materials have been utilized in energy harvesters, such as PZT (piezoelectric lead zirconate titanate) in meso- [8, 9] and

¹ The first two authors contributed equally to this work.

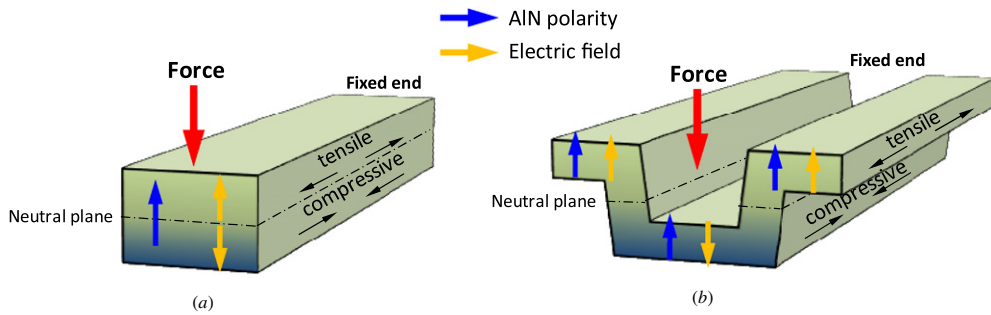


Figure 1. Schematic drawing of a single-piece piezoelectric cantilever with (a) rectangular-shaped cross section and (b) corrugated cross section.

micro-scales [7, 10, 11], aluminum nitride (AlN) in micro-scales [12], zinc oxide (ZnO) in nano-scale [13], and PVDF (polyvinylidene fluoride) at the meso- [14] and nano-scales [15]. Among these materials, PZT-based piezoelectric thin films have high electro-mechanical coupling coefficients and could produce the best energy conversion effectiveness for energy harvesters [16]. However, good quality PZT thin films require special and dedicated processes that are not easily achievable in thin-film depositions. Since extensive experiences on the fabrication of aluminum nitride micro-structures have been established in our laboratory for RF-MEMS components such as resonators [17] and filters [18], piezoelectric aluminum nitride has been selected as the piezoelectric demonstration material in this work.

Here a ‘corrugated’ structure is proposed to address the aforementioned design/manufacturing issues for improved energy conversion effectiveness in the field of piezoelectric micro energy harvesters. Two specific advancements have been accomplished in the design of piezoelectric energy harvesters: (1) a simple manufacturing process similar to the unimorph structure to reduce the manufacturing complexity; and (2) utilization of both top and bottom layers for piezoelectric energy generation similar to the bimorph designs for enhanced energy conversion effectiveness. Furthermore, aluminum nitride has been used as the piezoelectric material for consistent production of energy generation. The design, fabrication and testing of corrugated aluminum nitride energy harvesters are presented in detail including analytical and numerical simulation results and experimental validations for high energy conversion effectiveness.

2. Concept and analysis

2.1. Corrugated beam design

Figure 1 shows two piezoelectric cantilever beams with rectangular and corrugated cross sections, respectively. When force is applied at the free end of the cantilever, the stored strain energy above the neutral plane has the opposite sign to that below the neutral plane. The polarization direction of the piezoelectric layer is, in general, the same while using the same deposition process. Therefore, the electric fields generated due to the external force above and below the neutral plane are in opposite directions, as shown by the yellow arrows in the figures. If a beam contains only a single piezoelectric

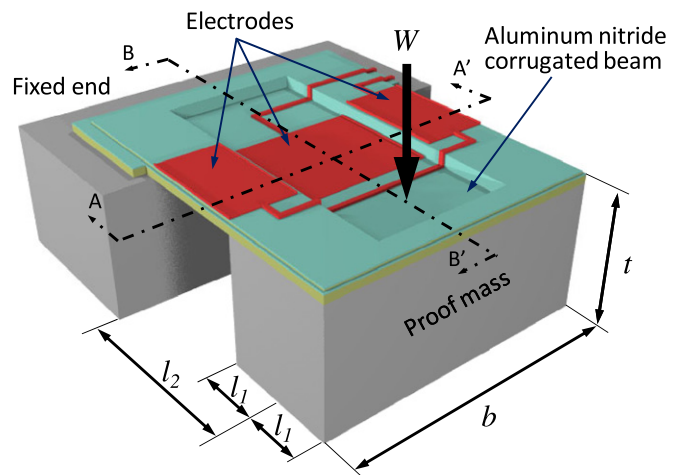


Figure 2. Schematic drawing of a piezoelectric energy harvester consisting of a cantilever supporting beam structure with a corrugated cross section.

layer with a rectangular cross section as in figure 1(a), the generated strain energy from the top and bottom piezoelectric layers could cancel each other out. Unimorph and bimorph designs have been utilized to prevent this cancellation effect. Specifically, a non-piezoelectric layer is used as a base layer in the unimorph design and a ‘thin middle electrode layer’ is sandwiched between two piezoelectric layers in the bimorph design. This work presents a new cantilever structural design with corrugated cross section made of a single piezoelectric layer as shown in figure 1(b). The total volume of the top piezoelectric structure is designed to be the same as the bottom one such that the neutral plane remains at the center. The generated electric fields above and below the neutral plane have opposite signs, but the generated energy from both the top and the bottom piezoelectric layers can be collected independently by proper electrode routings for better energy conversion effectiveness without complicating the manufacturing process.

Figure 2 shows the schematic drawing of the proposed energy harvesters based on the micromachining process consisting of a proof mass, a corrugated beam structure, electrodes, and electrical connection wires. The proof mass with a thickness of t is under a force, W , induced by acceleration (vibration) at a distance l_1 away from the end of the cantilever. The length from the center of the proof

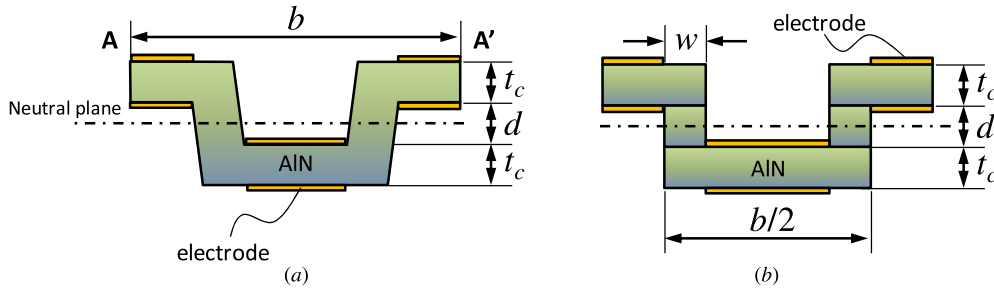


Figure 3. (a) Schematic drawing of the cross section along AA' in figure 2. (b) Modeling of the angled connecting parts as vertical sidewalls with width w .

mass to the starting point of the cantilever is defined as l_2 . The beam length is therefore $(l_2 - l_1)$. The width of the cantilever is defined as b and the neutral plane is designed at the center of the beam. When a bending force is applied, the electric power generated by this corrugated piezoelectric layer can be extracted out from both top and bottom piezoelectric layers independently through separated electrodes, without encountering the aforementioned cancellation problem. Furthermore, the corrugated design is reconfigurable as the resonance frequency, the footprint of the cantilever, and the size of the proof mass are all adjustable to match the specific vibration sources and applications.

The schematic drawing of the cross section along AA' in figure 2 is illustrated in figure 3(a). During the micromachining processes, the connecting parts between the top and bottom piezoelectric layers could have a small angle due to the etching process. In the theoretical modeling section, they are modeled as vertical sidewalls for simplicity, as shown in figure 3(b), where d is the thickness of the connecting parts between the bottom surface of the top piezoelectric layer and the top surface of the bottom piezoelectric layer, t_c is the thickness of the piezoelectric layer, and w is the sidewall deposition thickness (which is equal to t_c if the deposition is conformal). In this simplified model in figure 3(b), the bottom piezoelectric layer has the width of $b/2$ and the two top piezoelectric layers have the same width of $b/4$.

2.2. Moment of inertia

The energy conversion effectiveness of the piezoelectric device is estimated as the ratio of the generated electrical energy to the applied strain energy under a certain applied force. Since the resonance frequency and the applied force are both functions of external excitations, the energy conversion effectiveness should be compared under the same resonance frequency, applied force and device footprints based on the following assumptions.

- (1) The mechanical stiffness of the electrode layers is neglected due to small thickness.
- (2) Unimorph and bimorph designs are composed of different materials including piezoelectric and elastic layers, but their Young's modulus is assumed to be the same for structural comparison between different designs. However, this assumption is generally not valid for practical devices.

- (3) Piezoelectric beams of different cross sections (unimorph, bimorph and corrugated designs) are targeted to operate under the same environmental vibration frequency. It is assumed that they have the same proof mass, beam length, Young's modulus and deformation under the same external excitation. Therefore, the moments of inertia of these beams must have the same value.

The moment of inertia of the corrugated beam can be adjusted by changing the corrugation depth while keeping the same beam thickness. By neglecting the electrode stiffness based on assumption 1, the moment of inertia of a general corrugated structure with the distance of d shown in figure 3(b) can be described as

$$I_{\text{corr}} = 2 \times \left\{ \frac{bt_c^3}{24} + \frac{b \cdot t_c}{2} \left(\frac{d + t_c}{2} \right)^2 \right\} + \frac{wd^3}{6}. \quad (1)$$

If the distance d is set to be zero for better comparison with other cases, the moment of inertia of this corrugated structure becomes

$$I_{\text{corr},0} = \frac{bt_0^3}{3}, \quad (2)$$

where t_0 is the thickness of the piezoelectric layer without the connecting structures between the top and bottom piezoelectric layers. Based on assumption 3, the moment of inertia of all designs should be the same such that equation (1) is equal to equation (2) and the dimensions of the corrugated beam must satisfy

$$4\alpha^3 + 6\alpha^2\beta + 3\alpha\beta^2 + 2\gamma\beta^3 = 4, \quad (3)$$

where $\alpha = \frac{t_c}{t_0}$, $\beta = \frac{d}{t_0}$, $\gamma = \frac{w}{b}$.

For unimorph and bimorph designs, assumption 2 states that Young's modulus of the piezoelectric layer and the possible elastic layer are set as the same for simplicity. Figure 4(a) shows the cross-sectional view of a non-optimized ($t_p:t_e = 1:1$) unimorph structure, where t_{uni} is the total thickness of the structure, and t_p and t_e are the thicknesses of the piezoelectric layer and the inactive bottom elastic layer, respectively. Figure 4(b) shows a non-optimized bimorph structure with the same thickness t_b for the top and bottom piezoelectric layers. In the unimorph design, the thickness of the piezoelectric layer is half of the whole-beam thickness, that is, $t_p = t_{\text{uni}}/2 = t_b$. The moment of inertia of the unimorph and bimorph structure can be expressed as

$$I_{\text{uni}} = I_{\text{bi}} = \frac{2bt_b^3}{3}. \quad (4)$$

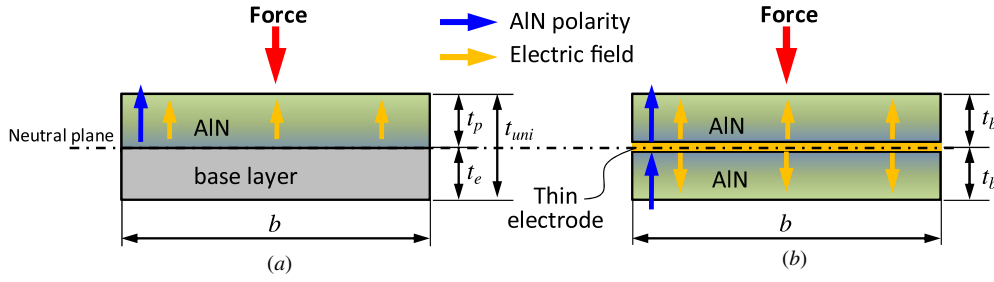


Figure 4. Cross sections of the conventional (a) unimorph and (b) bimorph energy harvester designs. A middle electrode is required in the bimorph design to extract electric fields above and below the neutral plane and its thickness is neglected in the simplified model.

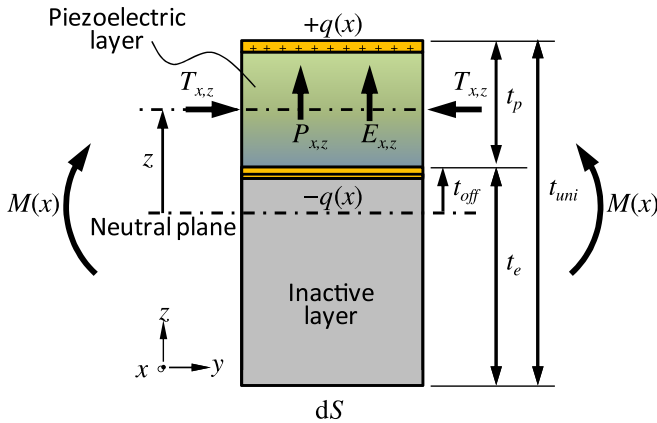


Figure 5. Unit element of a general unimorph structure.

Based on assumption 3, the relationship between t_0 and t_b can be defined by equalizing equations (2) and (4):

$$t_0^3 = 2t_b^3. \quad (5)$$

2.3. Capacitance energy in different structures

One can derive the generated capacitance energy by combining the piezoelectric equation and the strain energy together in the cantilever. Figure 5 is the schematic drawing of the unit element of a general unimorph cantilever where $M(x)$ is the applied bending moment, z is the distance from the neutral plane, $T_{x,z}$, $P_{x,z}$ and $E_{x,z}$ are the stress, the polarization and electric field at the location z , respectively, $q(x)$ is the electric charge, dS is the area of the electrode, t_p is the thickness of piezoelectric layer, and t_{off} is the offset of piezoelectric layer from the neutral plane. Since the polarization in a piezoelectric material is linear to the applied stress, the polarization can be expressed as

$$P_{x,z} = d_{31} T_{x,z} = d_{31} \frac{M(x)}{I_{uni}} z, \quad (6)$$

where I_{uni} is the moment of inertia and d_{31} is the transverse piezoelectric coefficient. The electric displacement $D_{x,z}$ can be described as

$$D_{x,z} = P_{x,z} + \varepsilon E_{x,z}, \quad (7)$$

where ε is the dielectric constant of the piezoelectric layer. Since the electric displacement satisfies the Maxwell equation,

the relation between the electric displacement and electric charge in the area from the bottom electrode to the height z is written as

$$D_{x,z} dS = -q(x). \quad (8)$$

Inserting equations (6) and (7) into equation (8) yields

$$d_{31} \frac{M(x)}{I_{uni}} z + \varepsilon E_{x,z} = -\frac{q(x)}{dS}. \quad (9)$$

Next, the electrode is assumed to cover the entire area of the unit element and its stiffness is ignored based on assumption 1. When the unit element is under an open circuit, the total electric charges in the electrode are conserved. Therefore, the integral of equation (9) must be equal to zero:

$$\int_0^b \int_{l_1}^{l_2} d_{31} \frac{M(x)}{I_{uni}} z + \varepsilon E_{x,z} dx dy = \int_0^b \int_{l_1}^{l_2} -\frac{q(x)}{dS} dx dy = 0. \quad (10)$$

Now assuming that the electric field is uniformly distributed in the electrodes and expressing the moment of inertia by the applied force W and the beam dimensions, equation (10) can be rewritten as

$$E_{x,z} = -\frac{d_{31} W z (l_2 + l_1)}{2\varepsilon I_{uni}}. \quad (11)$$

Since $E_{x,z}$ is constant along the x -axis, integrating equation (11) from the bottom (t_{off}) to the top ($t_{off} + t_p$) of the piezoelectric layer, one can derive the generated voltage for the unimorph piezoelectric beam:

$$\begin{aligned} V_{uni} &= \int_{t_{off}}^{t_{off}+t_p} E_{x,z} dz \\ &= -\frac{1}{4} \frac{d_{31}}{\varepsilon} \frac{W}{I_{uni}} \{ (t_{off} + t_p)^2 - t_{off}^2 \} (l_2 + l_1). \end{aligned} \quad (12)$$

Since the surface area of the unimorph beam is $b(l_2 - l_1)$, the capacitance energy can be expressed as

$$\begin{aligned} U_{uni} &= \frac{1}{2} C_{uni} V_{uni}^2 \\ &= \frac{1}{2} \frac{\varepsilon b (l_2 - l_1)}{t_p} \left[-\frac{1}{4} \frac{d_{31} W}{\varepsilon I_{uni}} \{ (t_{off} + t_p)^2 - t_{off}^2 \} (l_2 + l_1) \right]^2. \end{aligned} \quad (13)$$

From figure 5, we can write down the geometric relation of t_{uni} , t_e , t_p and t_{off} as

$$t_{uni} = t_e + t_p = 2(t_{off} + t_p) \quad \text{and} \quad t_p = \frac{t_{uni}}{2} - t_{off}. \quad (14)$$

Therefore, inserting equation (14) into equation (13) yields

$$U_{uni} = \frac{1}{32} \frac{d_{31}^2 W^2 b (l_2 - l_1) (l_2 + l_1)^2}{\epsilon I_{uni}^2} \times \left(t_{off} + \frac{t_{uni}}{2} \right)^2 \left(\frac{t_{uni}}{2} - t_{off} \right). \quad (15)$$

Taking the derivative of equation (15) over t_{off} , the optimized capacitance energy can be obtained when

$$\frac{t_{uni}}{2} - 3t_{off} = 0. \quad (16)$$

In other words, from equations (14) and (16), one can achieve the maximum capacitance energy from a unimorph design when the piezoelectric layer t_p is set as one-third of the total beam thickness, i.e. $t_p = 2t_{off}$.

The capacitance energy of a bimorph design, U_{bi} , is simply two times that of U_{uni} based on assumption 3 as a bimorph has two unimorph structures. As for the corrugated design, one can compare the unit element of the corrugated beam with the unimorph design, and replace the area of electrode by $b(1 - 2\gamma)(l_2 - l_1)$, t_{off} by $d/2$ and t_p by t_c , respectively, into equation (13) to derive the capacitance energy in a corrugated structure:

$$U_{corr} = \frac{1}{2} \frac{\epsilon b (1 - 2\gamma) (l_2 - l_1)}{t_c} \times \left[-\frac{1}{4} \frac{d_{31} W}{\epsilon I_{corr}} \left\{ \left(\frac{d}{2} + t_c \right)^2 - \left(\frac{d}{2} \right)^2 \right\} (l_2 + l_1) \right]^2, \quad (17)$$

which is a strong function of the distance d .

2.4. Normalized energy conversion effectiveness

The conversion effectiveness is defined by the ratio of the capacitance energy to the input strain energy. Since the moment of inertia and the mass are the same for all designs, the input strain energy should be the same when the same force is applied. Therefore, one can compare the energy conversion effectiveness of these structures by just comparing the capacitance energy instead. The normalized energy conversion effectiveness of corrugated beam is therefore

$$\frac{U_{corr}/U_{input}}{U_{uni}/U_{input}} = 2\alpha(\alpha + \beta)^2(1 - 2\gamma). \quad (18)$$

Figure 6 shows the normalized conversion effectiveness of the unimorph, bimorph and corrugated structures with respect to β . The sidewall thickness, w , was set to be equal to the AlN thickness t_c . The optimized unimorph ($t_p:t_e = 1:2$) and bimorph ($t_b:t_e:t_b = 1:1:1$) designs have 19% higher energy conversion effectiveness than their non-optimized cases. For the corrugated design, β is optimized at around 1.2–1.5, but starts to decrease afterward. Analytically, this is because the dimension of the connecting parts, which were not covered by electrodes, increases with β . However, the strain energy stored in these parts was not converted to electrical energy such that energy conversion effectiveness is reduced. When β is optimized, the corrugated design could achieve similar conversion effectiveness as the optimized bimorph structure. The same trend was also verified by the finite element analysis

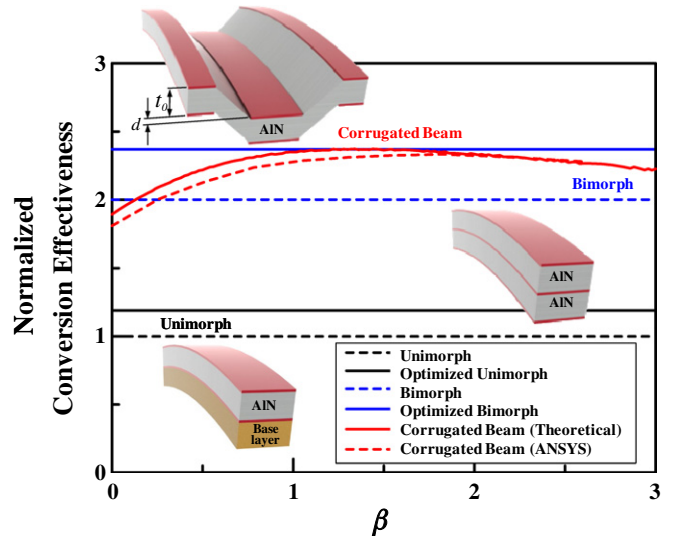


Figure 6. Normalized energy conversion effectiveness versus corrugation, β , which is defined as the ratio of the distance between the top and bottom parts and the thickness of the piezoelectric layer.

as shown. The numerical analyses predict a slightly lower energy conversion effectiveness for lower β values as the numerical model does include the tilted angle of 45° for the connecting parts, while the analytical model assumes vertical sidewalls for simplicity.

3. Fabrication process

Figure 7 shows the fabrication process flow of the corrugated beam energy harvester by means of silicon micromachining processes. The whole process is similar to the fabrication of a conventional unimorph energy harvester except one additional silicon groove-etching step to construct the corrugated cross section.

First, a groove was etched into the $680 \mu\text{m}$ thick silicon wafer by RIE (reactive ion etching) in figure 7(a), followed by a PECVD (plasma enhanced chemical vapor deposition) for a $0.5 \mu\text{m}$ thick silicon dioxide layer as the insulation and the etch-stop layer during the backside etching process. Afterward, a $0.1 \mu\text{m}$ thick Cr/Pt bottom electrode was deposited by sputtering and patterned by a lift-off process. Figure 7(b) applies after these steps.

Next, an *in situ* surface treatment of the bottom Pt electrode under low-power RF environment is conducted prior to AlN deposition to reduce the Pt surface roughness. A $2 \mu\text{m}$ thick piezoelectric AlN film was then deposited at 300°C using an ac reactive sputtering tool with a dual cathode S-Gun magnetron from Tegal Corporation as shown in figure 7(c). The columnar growth of AlN by this method is perpendicular to the growth surface. However, if there are slopes or sharp corners, the growth tends to have poor orientation and step coverage. Figure 8 shows the SEM image of the AlN deposition on the slope, where poor grain formation and voids were observed especially in designs with large connecting part thicknesses d . This problem could be alleviated with

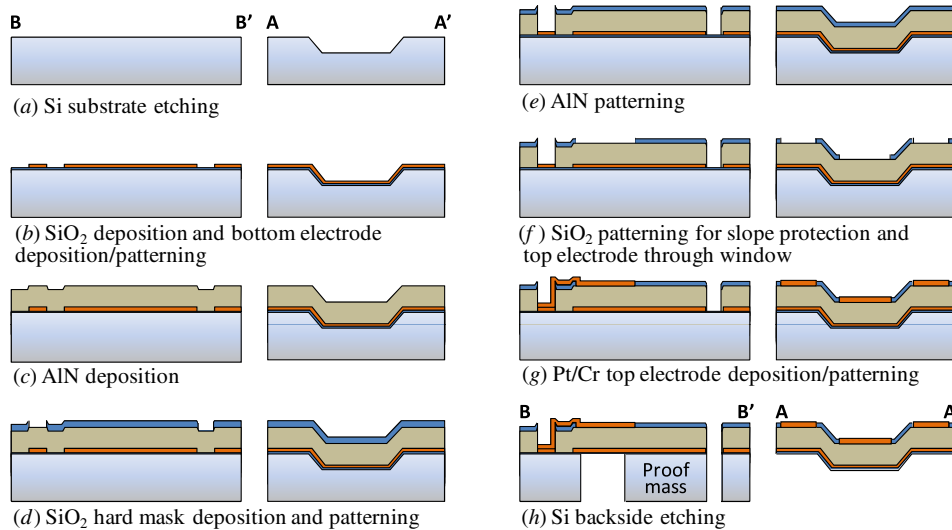


Figure 7. Fabrication process of the corrugated beam energy harvester which starts with the etching of the substrate as a template for the corrugated design. Only a single AlN deposition is required.

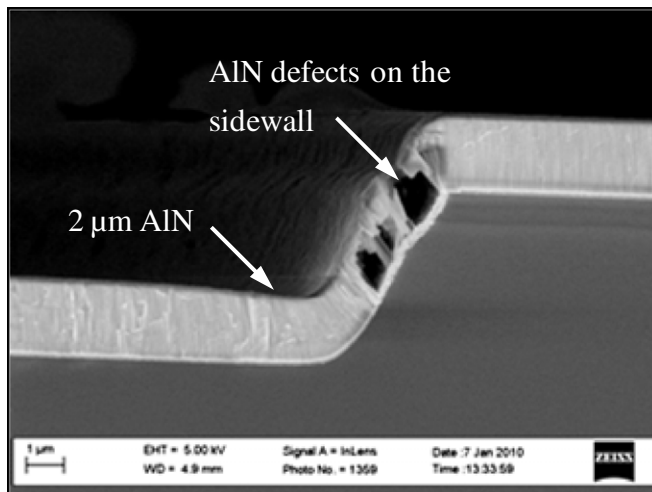


Figure 8. AlN defects/voids observed from deposition on a slope.

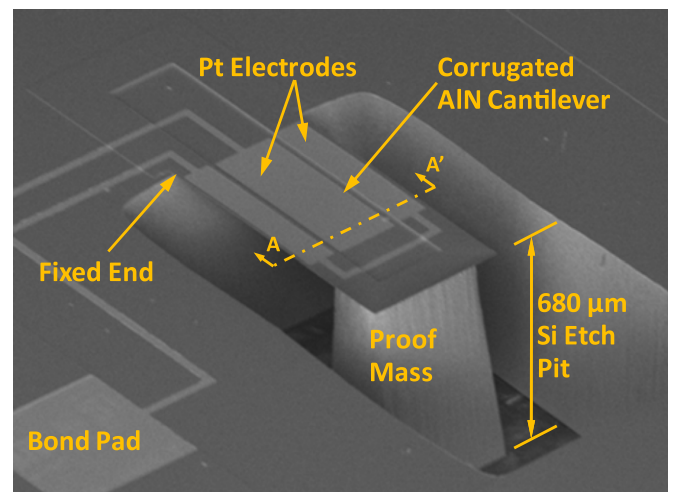


Figure 9. SEM image of an AlN corrugated beam energy harvester.

a smoother transitional design for the corrugated structures. Since only the capacitance energy stored in the top and bottom piezoelectric layers is calculated, these voids and defects should not affect the energy conversion effectiveness in the theoretical analyses. However, they could reduce the device reliability and stiffness to affect the measured energy conversion effectiveness.

After the AlN deposition, a $0.3 \mu\text{m}$ thick silicon dioxide layer was deposited and patterned as a hard mask as shown in figure 7(d) to etch AlN in 40°C TMAH for 10 min in figure 7(e). After the AlN etch process, this silicon dioxide hard mask was patterned to open the through window for the top electrode as shown in figure 7(f). In our design, the silicon dioxide layer around the corrugation area was also preserved to prevent undesired contact of top and bottom electrodes via the voids during the manufacturing process. The top electrode made of Cr/Pt was deposited and patterned on the AlN and also the through window to reach the bottom electrodes as shown in

figure 7(g). Finally, the proof mass was released by backside DRIE (deep reactive ion etching) silicon etching in figure 7(h). Figure 9 shows an SEM image of the corrugated beam energy harvester. The sidewall of the proof mass is not exactly vertical due to the backside DRIE etching process and this process could also cause slight under-cut (as shown in the photo) of the proof mass. As a result, these effects could change the volume of the proof mass and the length of the beam and shift the resonance frequency of the structure. The piezoelectric capacitance between top and bottom electrodes is established across the $2 \mu\text{m}$ thick AlN layer. Possible parasitic capacitance between the bonding pads would need to go across a distance of more than 1 mm in our prototype design. Therefore, the impact of the possible parasitic capacitance from the bonding pads is small and neglected.

Compared with the fabrication process of a unimorph structure, the additional step for fabricating the corrugated

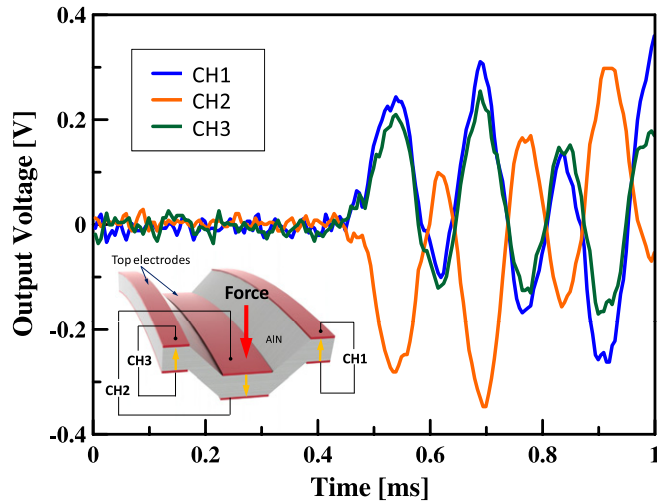


Figure 10. Output voltages of proposed energy harvester under a pulse input where channels 1 and 3 are connected to the top parts and channel 2 to the bottom part. Results validate the opposite direction of the generated electrical potential.

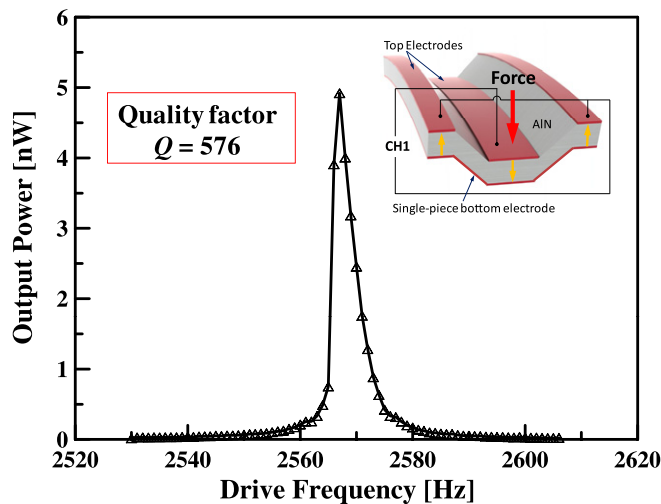


Figure 11. Output power versus drive frequency measured from a practical design utilizing a single-piece bottom electrode.

beam is the groove-etching step at the very beginning. This step requires one extra mask and is relatively easy to process.

4. Measurement and discussion

Two types of electrical connections have been designed and tested. The first one is the verification model, as illustrated in figure 10, where the bottom electrodes are divided into three parts to verify the polarity of the generated electric fields above and below the neutral plane of the piezoelectric layer. The second one is the practical model, as illustrated in figure 11, where the bottom electrodes are connected as a common potential to simplify the electrode routing and to maximize the output voltage.

In the first proof-of-concept experiment, the goal was to verify the basic concept of the corrugated design such that output voltages generated from separated electrodes were

collected as shown in figure 10. The dimensions of the silicon proof mass are $b = 400$, $2l_1 = 500$ and $t = 680 \mu\text{m}$. The dimensions of the corrugated beam are $b = 400 \mu\text{m}$ and $(l_2 - l_1) = 250 \mu\text{m}$ with the distance between top and bottom piezoelectric layers $d = 2.4 \mu\text{m}$. In order to verify the polarity of electric fields at each part of the piezoelectric layer, channels 1 and 3 are connected to the top parts of the corrugated AlN layer while channel 2 is connected to the bottom part. This prototype device was aligned and attached to a custom-made PCB (printed-circuit board), which has one $5 \times 5 \text{ mm}^2$ through hole to allow the free up and down movement of the proof mass. Electrical connections were connected via aluminum wire-bonds from the bonding pads to the PCB. Mechanical excitation was manually applied by using the human finger to excite the whole PCB such that the excitation time, amplitude and shape were poorly controlled. Nevertheless, one can clearly identify the relatively same voltage outputs from channels 1 and 3 and the opposite polarity of channel 2 in the voltage–time plot. Since the AlN polarization is in the $[001]$ direction, the symmetric voltage readout from the top and the bottom of the corrugated beam validated that the neutral plane locates around the middle as designed and opposite generated electric fields can be extracted from each piezoelectric area without the need of the inactive base layer.

Next, a practical design with the same proof mass and beam dimensions but with $d = 4.68 \mu\text{m}$ was mounted on a vibration stage and the relationship between the output power and drive frequency was plotted in figure 11. The resonance frequency of this device was observed at 2.56 kHz. When an input acceleration of 0.25 G was applied, the amplitude of output voltage was recorded as 92 mV at a load resistance of $0.86 \text{ M}\Omega$. Therefore, the calculated output power of this device is 4.9 nW. The theoretical maximum output power P_m [19] from the vibration energy harvester can be expressed as

$$P_m = \frac{2MY_0^2\omega^3Q}{\pi}, \quad (19)$$

where M is the mass of the proof mass, Y_0 is the amplitude of the input vibration, ω is the angular velocity and Q is the quality factor. With a Q of 576 obtained from figure 11 and M of 0.31 mg from the calculated volume and density of silicon, the theoretical maximum power is 43 nW and 11.4% conversion effectiveness of this device was calculated.

Analytically, the stiffness of the mass–beam model can be derived by calculating the total strain energy of the system and taking partial derivative with respect to the applied force (Castigliano’s theorem) as

$$K = \frac{3YI_{\text{corr}}}{l_2^3 - l_1^3}, \quad (20)$$

where Y is Young’s modulus of the corrugated beam and I_{corr} is the moment of inertia as discussed in equation (1). The resonance frequency is therefore

$$f = \frac{1}{2\pi} \sqrt{\frac{K}{M}}, \quad (21)$$

where M is the mass of the proof mass and K is the stiffness as presented in equation (20). By using equations (20) and

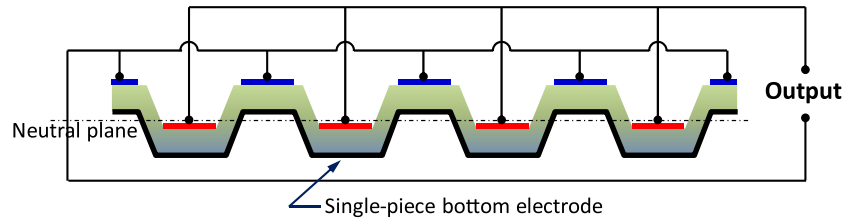


Figure 12. A multifold design of the corrugated cross-section beam with a single-piece bottom electrode.

(21), the predicted resonance frequency of this device shown in figure 11 is 2.50 kHz. The difference between the measured and predicted resonance frequencies comes mainly from (1) defects/voids in the connecting parts of the AlN corrugated structure between the top and bottom layers, and (2) the over-etching of silicon substrate during the silicon DRIE process. Defects and voids could lower the stiffness of the beam as well as the resonance frequency. The under-cut of proof mass due to the over-etching process could reduce the size of the proof mass and result in higher resonance frequency. On the other hand, if the cantilever beam length is increased due to over-etching of silicon, the resonance frequency of the device should become lower. For the prototype device in figure 11, the measured resonance frequency of the fabricated structure is higher than the predicted value and this implies that the effect of 'reduction in proof mass' is stronger than other effects in favor of higher resonance frequency.

It is worth mentioning that the distance d affects not only the conversion effectiveness but also the resonance frequency of the energy harvester. Since the resonance frequency of the device is proportional to the square root of the moment of inertia, d is an important design parameter to determine the resonance frequency without changing other dimensions of the device. A device with the same footprint as demonstrated in figure 11 but different d of $2.4 \mu\text{m}$ has also been measured and the resonance frequency is lowered to 1.55 kHz due to the smaller d value. Voids and defects of AlN were observed in some designs with steep slopes. Even with these voids, the current prototype structures did not show any signs of degradations or frequency shifts during the 60 min tests operating around its resonance frequency.

In order to obtain higher output power, one can design a corrugated beam with larger area or a multi-fold, large-footprint corrugated cantilever as illustrated in figure 12. Compared with the onefold device mentioned in figure 11, the multifold design alleviates the stress issue in the width direction. For the prototype design, the proof mass dimensions are $b = 2400$, $2l_1 = 500$ and $t = 680 \mu\text{m}$, and the AlN corrugated beam dimensions are $b = 2400$, $(l_2 - l_1) = 500$ and $d = 4.68 \mu\text{m}$. The recorded output power is $0.17 \mu\text{W}$ under an acceleration of 1 G. The resonance frequency was measured at 853 Hz with an optimized load resistance of $1.1 \text{M}\Omega$. The nonlinear effect from this device has been observed as shown in figure 13. The output power from downward frequency sweep shows a lower resonance frequency at 794 Hz with a higher output power up to $0.55 \mu\text{W}$. During the downward frequency sweep, the output power has been observed to be constant under 0.5, 0.75 and 1 G inputs.

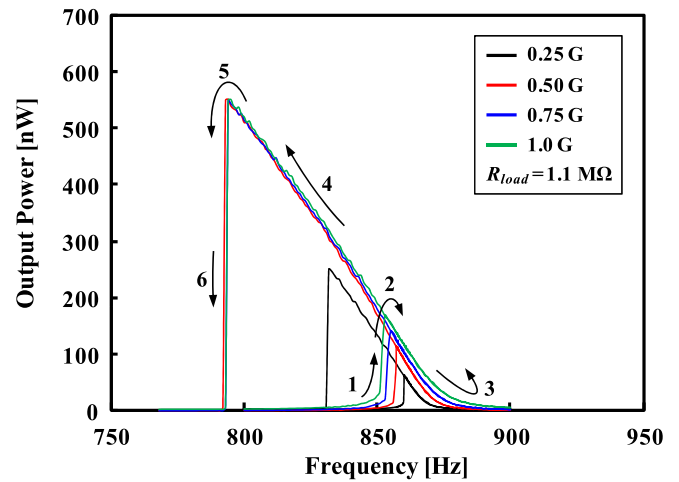


Figure 13. Nonlinearity effects observed from multifold devices. 1–3 are up-sweeps and 4–6 are down-sweeps.

However, under 0.25 G acceleration input, the maximum power reduced to about $0.25 \mu\text{W}$. One possible explanation is that under higher acceleration inputs, the nonlinear spring from the slanted connecting parts in the corrugated beam could reach a saturated minimum value to have the same effective value. This spring constant reduces while the bending force is increased and reaches its minimum while the corrugated beam flattens out. On the other hand, during the upward frequency sweeps, the maximum output power increased as the input acceleration magnitudes increased as shown. Further studies on both analytical modeling and measurements are necessary to provide better understanding of these nonlinear effects. Nevertheless, these preliminary results validate the basic concept of corrugated beam design by using a simple manufacturing process with AlN as the piezoelectric material.

5. Conclusion

Corrugated MEMS piezoelectric energy harvesters have been designed and fabricated with experimental validations and characterizations. As presented, corrugated energy harvesters have the advantages of a simple fabrication process similar to the unimorph beam design to achieve high energy conversion effectiveness comparable to the bimorph beam design. The generated electric fields above and below the neutral plane have been experimentally measured to have the opposite polarities under a pulsed acceleration input and the generated energy could be extracted independently without the common

cancellation problem in a single piezoelectric beam design. The distance d between the top and bottom piezoelectric layers of the corrugated structure is an important design factor to maximize the energy conversion effectiveness and to establish a specific resonance frequency for the device. A prototype multifold device resonating at 853 Hz with output power of $0.17 \mu\text{W}$ under the acceleration of 1 G has been recorded with nonlinear output power with respect to the input acceleration frequencies. It is believed that the slanted connecting parts in the corrugated beam structure introduce nonlinear spring effects. Although these devices have been fabricated on the silicon substrate and tested in the benign environment, superb material properties of AlN could provide an alternative solution to scavenge vibration energy from harsh environments for advanced microsensors systems.

Acknowledgments

These devices have been fabricated at the Berkeley Marvell Nanofabrication Laboratory. The authors would like to thank members in the Berkeley Marvell Nanofabrication Laboratory for assistance, including Dr Elizabeth Reilly for assisting the measurement setup, Dr David Myers for insightful discussions on the corrugated structure, Lindsay Miller and Gabriele Vigevani for sharing their fabrication knowledge and Chris Xu Zhao for AlN thin film characterization.

References

- [1] Roundy S and Wright P K 2004 A piezoelectric vibration based generator for wireless electronics *Smart Mater. Struct.* **13** 1131–42
- [2] Platt S R, Farritor S and Haider H 2005 On low-frequency power generation with PZT ceramics *IEEE/ASME Trans. Mechatronics* **10** 240–52
- [3] Roundy S, Leland E S, Baker J, Carleton E, Reilly E, Lai E, Otis B, Rabaey J M, Wright P K and Sundararajan V 2005 Improving power output for vibration-based energy scavengers *IEEE Pervasive Comput.* **4** 28–36
- [4] Mateu L and Moll F 2005 Optimum piezoelectric bending beam structures for energy harvesting using shoe inserts *J. Intell. Mater. Syst. Struct.* **16** 835–45
- [5] Erturk A and Inman D J 2009 An experimentally validated bimorph cantilever model for piezoelectric energy harvesting from base excitations *Smart Mater. Struct.* **18** 025009
- [6] Fang H-B, Liu J-Q, Xu Z-Y, Dong L, Wang L, Chen D, Cai B-C and Liu Y 2006 Fabrication and performance of MEMS-based piezoelectric power generator for vibration energy harvesting *Microelectron. J.* **37** 1280–4
- [7] Shen D, Park J-H, Ajitsaria J, Choe S-Y, Wickle H C III and Kim D-J 2008 The design, fabrication and evaluation of a MEMS PZT cantilever with an integrated Si proof mass for vibration energy harvesting *J. Micromech. Microeng.* **18** 055017
- [8] Kok S L, White N M and Harris N R 2008 A free-standing, thick-film piezoelectric energy harvester *IEEE Sensors Conf.* pp 589–92
- [9] Mathers A, Moon K S and Yi J 2009 A vibration-based PMN-PT energy harvester *IEEE Sensors J.* **9** 731–9
- [10] Jeon Y B, Sood R, Jeong J-H and Kim S-G 2005 MEMS power generator with transverse mode thin film PZT *Sensors Actuators A* **122** 16–22
- [11] Knight R R, Mo C and Clark W W 2009 Development and testing of a MEMS piezoelectric energy harvester *Proc. SPIE* **7288** 72880A-1
- [12] Elfrink R, Kamel T M, Goedbloed M, Matova S, Hohlfeld D, van Andel Y and van Schaijk R 2009 Vibration energy harvesting with aluminum nitride-based piezoelectric devices *J. Micromech. Microeng.* **19** 094005
- [13] Lu M-P, Song J, Lu M-Y, Chen M-T, Gao Y, Chen L-J and Wang Z L 2009 Piezoelectric nanogenerator using p type ZnO nanowire arrays *Nano Lett.* **9** 1223–7
- [14] Li S, Yuan J and Lipson H 2011 Ambient wind energy harvesting using cross-flow fluttering *J. Appl. Phys.* **109** 026104
- [15] Chang C, Tran V H, Wang J, Fuh Y-K and Lin L 2010 Direct-write piezoelectric polymeric nanogenerator with high energy conversion efficiency *Nanoletters* **10** 726–31
- [16] Fujii E, Takayama R, Nomura K, Murata A, Hirasawa T, Tomozawa A, Fujii S, Kamada T and Torii H 2007 Preparation of (0 0 1)-oriented Pb(Zr,Ti)O₃ thin films and their piezoelectric applications *IEEE Trans. Ultrason. Ferroelectr. Freq. Control* **54** 2431–8
- [17] Lin C-M, Yen T-T, Felmetser V V, Hopcroft M A, Kuypers J H and Pisano A P 2010 Thermally compensated aluminum nitride Lamb wave resonators for high temperature applications *Appl. Phys. Lett.* **97** 083501
- [18] Yen T-T, Lin C-M, Hopcroft M A, Kuypers J H, Senesky D G and Pisano A P 2010 Synthesis of narrowband AlN Lamb wave ladder-type filters based on overhang adjustment *IEEE International Ultrasonic Symposium* 970–3
- [19] Mitcheson P D, Reilly E K, Toh T, Wright P K and Yeatman E M 2007 Performance limits of the three MEMS inertial energy generator transduction types *J. Micromech. Microeng.* **17** S211–6